Inorg. Chem. **2006**, *45*, 4642–4653

Synthesis, Characterization, and DFT-TDDFT Computational Study of a Ruthenium Complex Containing a Functionalized Tetradentate Ligand

C. Barolo,[†] Md. K. Nazeeruddin,*[,‡] Simona Fantacci,*[,‡] D. Di Censo, P. Comte, P. Liska, G. Viscardi,[†] P. Quagliotto,[†] Filippo De Angelis,[‡] S. Ito, and M. Grätzel*

Laboratory for Photonics and Interfaces, Institute of Chemical Sciences and Engineering, School of Basic Sciences, Ecole Polytechnique Fédérale de Lausanne, Station 6, CH-1015 Lausanne, Switzerland, and Istituto CNR di Scienze e Tecnologie Molecolari (ISTM-CNR), c/o Dipartimento di Chimica, Università di Perugia, via Elce di Sotto 8, I-06213 Perugia, Italy

Received November 14, 2005

A ruthenium complex *trans*-[Ru(L)(NCS)$_2$], L = 4,4‴-di-*tert*-butyl-4′,4″-bis(carboxylic acid)-2,2′:6′,2″:6″,2‴-quaterpyridine (N886), was synthesized and characterized by spectroscopic and electrochemical methods. The absorption spectrum of the N886 complex shows metal-to-ligand charge-transfer transitions in the entire visible region and quasi-reversible oxidation and reduction potentials at $E_{1/2}$ = +0.38 and −1.92 V vs ferrocene, respectively. The electronic spectra of the N886 complex were calculated by density functional theory (DFT)–time-dependent DFT, which qualitatively reproduces the experimental absorption spectra for both the protonated and deprotonated species. From the analysis of the computed optical transitions of N886, we assign its absorption bands as mixed Ru/SCN-to-quaterpyridine charge-transfer transitions, which extend from the near-IR to the UV regions. The panchromatic response of the N886 complex renders it as a suitable sensitizer for solar energy conversion applications based on titanium dioxide mesoporous electrodes. The preliminary results using the N886 complex as a sensitizer in a dye-sensitized solar cell, with an electrolyte containing 0.60 M butylmethylimidazolium iodide, 0.03 M I_2, and 0.50 M *tert*-butylpyridine in a mixture of acetonitrile and valeronitrile (volume ratio 1:1), show 40% incident photon-to-current efficiencies, yielding under standard AM 1.5 sunlight a short-circuit photocurrent density of 11.8 ± 0.2 mA/cm^2, an open-circuit voltage of 680 ± 30 mV, and a fill factor of 0.73 ± 0.03, corresponding to an overall conversion efficiency of 5.85%.

1. Introduction

The development of dye-sensitized solar cells comes out of an interest in artificial photosynthesis.[1] The prototype energy-absorbing dye provided by nature is chlorophyll, the molecule consisting of a central magnesium atom surrounded by four nitrogen-containing flat porphyrin rings. Although nature confines itself to magnesium, the whole range of metallic elements is available for the synthesis of flat types of dyes. Among them, the use of ruthenium metal is particularly attractive because of its octahedral coordination geometry, where one can introduce specific ligands in a controlled manner to tune the photophysical, photochemical, and electrochemical properties.[2] The *cis*-dithiocyanatobis-(2,2′-bipyridyl-4,4′-dicarboxylic acid)ruthenium(II) complex (N3) is one of the most efficient heterogeneous charge-transfer sensitizers and is widely used in the nanocrystalline TiO_2-based dye-sensitized solar cell.[3−25] Efficient charge transfer occurs after anchoring of the sensitizer through an

* To whom correspondence should be addressed. E-mail: MdKhaja.Nazeeruddin@epfl.ch (M.K.N.), simona@thch.unipg.it (S.F.), michael.graetzel@epfl.ch (M.G.).

[†] Dipartimento di Chimica Generale ed Organica Applicata, Centre of Excellence for Nanostructured Interfaces and Interfaces, Università di Torino, Corso Massimo D'Azeglio 48, 10125 Torino, Italy.

[‡] Present address: Istituto CNR di Scienze e Tecnologie Molecolari (ISTM-CNR), Dipartimento di Chimica, Università di Perugia, via Elce di Sotto 8, I-06213 Perugia, Italy.

(1) Grätzel, M. *CATTECH* **1999**, *3*, 4.

(2) Juris, A.; Balzani, V.; Barigelletti, F.; Campagna, S.; Belser, P.; von Zelewsky, A. *Coord. Chem. Rev.* **1988**, *84*, 85.

(3) Grätzel, M. *Nature* **2001**, *414*, 338.

(4) *Special Issue: Michael Graetzel Festschrift, A tribute for this 60th Birthday: Dye Sensitized Solar Cells*; Nazeeruddin, M. K., Ed.; Elsevier: Amsterdam, The Netherlands, 2004; Vol. 248.

(5) Asbury, J. B.; Ellingson, R. J.; Gosh, H. N.; Ferrere, S.; Notzig, A. J.; Lian, T. *J. Phys. Chem. B* **1999**, *103*, 3110.

(6) Park, N.-G.; Kang, M. G.; Kim, K. M.; Ryu, K. S.; Chang, S. H.; Kim, D.-K.; Van de Lagemaat, J.; Benkstein, K. D.; Frank, A. J. *Langmuir* **2004**, *20*, 4246.

10.1021/ic051970w CCC: $33.50
Published on Web 05/10/2006

acid carboxylate group to the surface of the semiconductor. The immobilized sensitizer forms a monomolecular film on the semiconductor substrate, thereby facilitating charge transfer by electron injection.[26]

The majority of the ruthenium complexes reported to date containing two bipyridyl and two monodentate ligands have a cis configuration and show absorption in the visible region at around 535 nm. Essential for efficient conversion of incident radiation by any photovoltaic system is the spectral match of the sensitizer absorption spectra to the incident light, and in this regard, the N3 dye is inadequate. Therefore, development of complexes with extended absorption spectral sensitivity into the IR region is essential.[27] A strategy that has been adopted resides in the structural modification of the complex; indeed, geometrical isomerism can lead to complexes with variant optical properties.[28] For example, the standard N3 shows a cis arrangement of the two thiocyanate ligands; the corresponding trans isomer has an extended sensitivity into the IR region of the visible spectrum.[28] Nevertheless, a drawback of the use of trans complexes is their thermal and photoinduced isomerization back to the cis configuration.

Thus, the ideal solution would be to design ligands that stabilize the trans configuration, whose spectral sensitivity extends throughout the visible and into the IR region, approaching the ideal absorption edge position (1.4 eV) for optimal solar energy conversion.[29,30] The application of a tetradentate ligand inhibits the trans → cis isomerization process, and the axial coordination sites are used further to fine-tune the spectral and redox properties.[31] In this contest, we synthesized and characterized a *trans*-[Ru(L)$(NCS)_2$], L = 4,4‴-di-*tert*-butyl-4′,4″-bis(carboxylic acid)-2,2′:6′,2″:6″,2‴-quaterpyridine (N886), complex. This paper presents a detailed account of the synthesis, characterization, and comparison of experimental and theoretical spectral properties of this *trans*-quaterpyridineruthenium complex.

2. Experimental Section

2.1. Materials and Methods. All of the solvents and chemicals, unless stated otherwise, were purchased from Fluka, puriss grade. 4,4′-Dimethyl-2,2′-bipyridine, dichloro(*p*-cymene)ruthenium(II) dimer, and potassium/ammonium thiocyanate were obtained from Aldrich and used as received. Thin-layer chromatography was carried out using Merck silica gel 60 F_{254} plates. Column chromatography purifications were performed by flash chromatography using silica gel (Merck, 40−63 mm). Samples were applied as a saturated solution in an appropriate solvent or were preadsorbed onto a small quantity of silica.

UV−vis spectra were recorded in 95% ethanol on a Pye Unicam UV2 and/or Cary 5 spectrophotometer in a 1-cm-path-length quartz cell. IR spectra were recorded as KBr disks or in a solid-phase powder using an ATR-FTIR Shimadzu spectrometer 8400 or Digilab 7000. The ATR data reported here were taken with the "Golden Gate" diamond-anvil ATR accessory (Graseby-Specac) typically using 64 scans at a resolution of 2 cm^{-1}. The IR optical bench was flushed with dry air. The FTIR spectra of anchored dyes were obtained by subtracting the IR spectrum of the blank TiO_2 films from the IR spectrum of the dye-coated TiO_2 films of the same thickness. ^1H NMR spectra were measured on a Bruker 200 MHz or a JEOL EX400 NMR spectrometer in DMSO-d_6, using the DMSO signal as a reference (2.50 ppm, ^1H), in $CDCl_3$, using the $CHCl_3$ signal as a reference (7.26 ppm, ^1H), or in CD_3OD, using the CH_3OH signal as a reference (3.35 ppm, ^1H). Signals are described as singlets (s), broad (br), doublets (d), triplets (t), quartets (q), multiplets (m), double doublets (dd), and double double doublets (ddd). Mass spectra (MS) [electron impact or chemical ionization (CI)] were recorded on a Thermo Finnigan Trace GC−MS^{PLUS} instrument Mat.

Electrochemical data were obtained by cyclic and square-wave voltammetry using a PC-controlled AutoLab system (PGSTAT30, Eco Chimie), where a glassy carbon disk working electrode, a silver coil auxiliary electrode, and a silver wire quasi-reference electrode were mounted in a single-compartment-cell configuration. A cyclic voltammogram (CV) of the N886 complex was obtained by dissolving 1 mM of the complex in *N*,*N*-dimethylformamide (DMF) containing 0.1 M tetrabutylammonium perchlorate as the supporting electrolyte. After the measurement, ferrocene (Fc) was added as an internal reference for calibration of the other redox couple potentials versus the value relative to the Fc^+/Fc couple.

Photoelectrochemical data were measured using a 450-W xenon light source that was focused to give 1000 W/m^2, the equivalent of

(7) Heimer, T. A.; Heilweil, E. J.; Bignozzi, C. A.; Meyer, G. J. *J. Phys. Chem. A* **2000**, *104*, 4256.
(8) Lee, J.-J.; Coia, G. M.; Lewis, N. S. *J. Phys. Chem B* **2004**, *108*, 5269.
(9) Saito, Y.; Fukuri, N.; Senadeera, R.; Kitamura, T.; Wada, Y.; Yanagida, S. *Electrochem. Commun.* **2004**, *6*, 71.
(10) Kamat, P. V.; Haria, M.; Hotchandani, S. *J. Phys. Chem B* **2004**, *108*, 5166.
(11) Qiu, F. L.; Fisher, A. C.; Walker, A. B.; Petecr, L. M. *Electrochem. Commun.* **2003**, *5*, 711.
(12) Nazeeruddin, M. K.; Humphry-Baker, R.; Liska, P.; Grätzel, M. *J. Phys. Chem. B* **2003**, *127*, 8981.
(13) Adachi, M.; Murata, Y.; Takao, J.; Jiu, J.; Sakamoto, M.; Wang, F. *J. Am. Chem. Soc.* **2004**, *126*, 14943.
(14) Argazzi, R.; Larramona, G.; Contado, C.; Bignozzi, C. A. *J. Photochem. Photobiol., A* **2004**, *164*, 15.
(15) Bisquert, J.; Cahen, D.; Hodes, G.; Ruehle, S.; Zaban, A. *J. Phys. Chem. B* **2004**, *108*, 8106.
(16) Cao, J.; Sun, J.-Z.; Hong, J.; Yang, X.-G.; Chen, H.-Z.; Wang, M. *Appl. Phys. Lett.* **2003**, *83*, 1896.
(17) Durr, M.; Bamedi, A.; Yasuda, A.; Nelles, G. *Appl. Phys. Lett.* **2004**, *84*, 3397.
(18) Fabregat-Santiago, F.; Garcia-Canadas, J.; Palomares, E.; Clifford, J. N.; Haque, S. A.; Durrant, J. R.; Garcia-Belmonte, G.; Bisquert, J. *J. Appl. Phys.* **2004**, *96*, 6903.
(19) Figgemeier, E.; Hagfeldt, A. *Int. J. Photoenergy* **2004**, *6*, 127.
(20) Furube, A.; Katoh, R.; Yoshihara, T.; Hara, K.; Murata, S.; Arakawa, H.; Tachiya, M. *J. Phys. Chem. B* **2004**, *108*, 12588.
(21) Hongwei, H.; Xingzhong, Z.; Jian, L. *J. Electrochem. Soc.* **2005**, *1*, 152.
(22) Kim, J. H.; Kang, M.-S.; Kim, Y. J.; Won, J.; Park, N.-G.; Kang, Y. S. *Chem. Commun.* **2004**, 1662.
(23) Miyasaka, T.; Kijitori, Y. *J. Electrochem. Soc.* **2004**, *151*, A1767.
(24) Nazeeruddin, M. K.; Humphry-Baker, R.; Officer, D. L.; Campbell, W. M.; Burrell, A. K.; Graetzel, M. *Langmuir* **2004**, *20*, 6514.
(25) Xue, B.; Wang, H.; Hu, Y.; Li, H.; Wang, Z.; Meng, Q.; Huang, X.; Sato, O.; Chen, L.; Fujishima, A. *Photochem. Photobiol. Sci.* **2004**, *3*, 918.
(26) Nazeeruddin, M. K.; Kay, A.; Rodicio, I.; Humphry-Baker, R.; Muller, E.; Liska, P.; Vlachopoulos, N.; Grätzel, M. *J. Am. Chem. Soc.* **1993**, *115*, 6382.
(27) Nazeeruddin, M. K.; Pechy, P.; Grätzel, M. *Chem. Commun.* **1997**, 1705.
(28) Nazeeruddin, M. K.; Zakeeruddin, S. M.; Humphry-Baker, R.; Gorelsky, S. I.; Lever, A. B. P.; Grätzel, M. *Coord. Chem. Rev.* **2000**, *208*, 213.
(29) Haught, A. F. *J. Sol. Energy Eng.* **1984**, *106*, 3.
(30) De Vos, A. *Endoreversible Thermodynamics of Solar Energy Conversion*; Oxford Science Publishers: Oxford, U.K., 1992; Chapter 6.
(31) Renouard, T.; Fallahpour, R.-A.; Nazeeruddin, M. K.; Humphry-Baker, R.; Gorelsky, S. I.; Lever, A. B. P.; Grätzel, M. *Inorg. Chem.* **2002**, *41*, 367.

Scheme 1. Retrosynthesis of a Series of Quaterpyridines

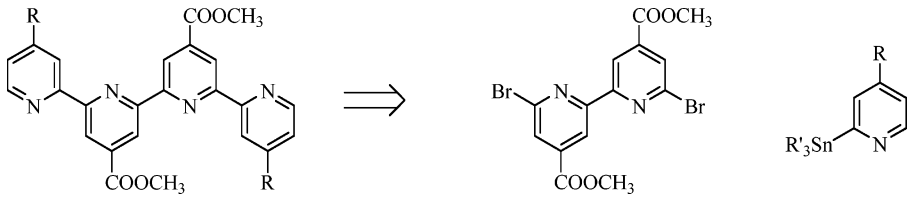

one sun at air mass 1.5, at the surface of the test cell. The screen-printed double-layer film consisted of a 8-mm transparent layer and a 4-mm scattering layer whose thickness was determined by using an Alpha-step 200 surface profilometer (Tencor Instruments, San Jose, CA). The electrodes were treated with a 0.05 M titanium tetrachloride solution using a previously reported procedure.[32] The film was heated to 500 °C in air and calcined for 20 min before use. Dye solutions were prepared in the concentration range of (2−3) × 10^{-4} M in a 1:1 (v/v) acetonitrile/*tert*-butyl alcohol solution, and the electrodes were dipped into the dye solution for 15−18 h. The dye-coated electrodes were rinsed quickly with acetonitrile and used as such for photovoltaic measurements. The fabrication procedure for solar cells, the testing conditions, and the equipment used were reported before.[12]

2.2. Synthesis and Characterization. Synthesis of Dimethyl 4,4‴-Di-*tert*-butyl-2,2′;6,2″;6″2‴-quaterpyridine-4′,4″-dicarboxylate. The ligand was synthesized by reacting dimethyl 6,6′-dibromo-2,2′-bipyridine-4,4′-dicarboxylate (compound **3** in the Supporting Information) and 4-*tert*-butyl-2-(tributylstannanyl)-pyridine (compound **6b** in the Supporting Information) using the following conditions. The reaction was performed in a well-dried round-bottomed flask equipped with a reflux condenser in an argon atmosphere. To a solution of compound **3** (1 g, 2.3 mmol) in freshly distilled anhydrous toluene (30 mL) was added dropwise a toluene solution of **6b** (2.12 g, 5.8 mmol). $Pd(PPh_3)_4$ (0.018 mmol) was added to this solution, and the reaction mixture was heated at reflux for 72 h. The solution was allowed to cool to room temperature, and the excess of the solvent was removed in vacuo. The crude product was purified by column chromatography (1:1 ethyl acetate/petroleum ether) or crystallized in chloroform/diethyl ether to give the title compound (1.23 g, 90%) as an off-white powder.

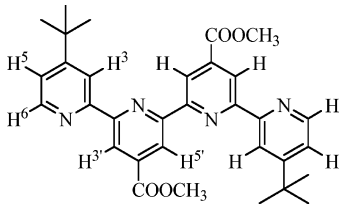

^{1}H NMR (400 MHz, $CDCl_3$): δ 9.2 (s, 2H, $H^{3'}$), 9.02 (s, 2H, H^3), 8.74 (s, 2H, $H^{5'}$), 8.65 (d, 2H, H^6), 7.39 (d, 2H, H^5), 4. 03 (s, 6H, O−CH_3), 1.43 (s, 18H, C−CH_3). IR (ATR): 3083 (w, C−H st Ar), 2954−2866 (w, C−H st Al), 1730 (s n, C═O st Est), 1588−1547 (m n, C═C, C═N Ar), 1479 (m, C−H bend *tert*-butyl), 1369−1353 (m d, C−H bend CH_3 *tert*-butyl), 1266−1224 (s n, C−O st) cm^{-1}. CIMS (Thermo Finnigan Trace GC−MS^{PLUS}): 538 (M^+) 523, 507, 481, 233 (100%) uma.

Synthesis of *trans*-Dithiocynato[ruthenium (4,4‴-di-*tert*-butyl-4′,4″-dicarboxy-2,2′;6,2″;6″,2‴-quaterpyridine)] (N886). A mixture of ligand dimethyl 4,4‴-di-*tert*-butyl-2,2′;6,2″;6″,2‴-quaterpyridine-4′,4″-dicarboxylate (0.192 g, 0.4 mM) and a dichloro(*p*-cymene)ruthenium(II) dimer (0.12 g, 0.2 mM) in argon-degassed DMF (50 mL) was refluxed for 4 h under reduced light. After this was added ammonium thiocyanate (0.304 g, 4 mM), and the solution was refluxed for a further 4 h at 140 °C. Then, 20 mL of triethylamine and 10 mL of water were added, and the solution was refluxed for a further 24 h to hydrolyze the ester groups on the quaterpyridine ligand. The DMF solvent was evaporated, and to the resulting purple residue was added water (15 mL); the mixture was allowed to stand in a refrigerator overnight at −4 °C. The resulting solid was then filtered and successively washed with water and diethyl ether.

The crude N886 complex was dissolved in methanol (5 mL) containing 2 equiv of tetrabutylammonium hydroxide to confer solubility by deprotonating the carboxylic group. The concentrated solution was filtered through a sintered glass crucible (G4) and charged onto a Sephadex LH-20 column, which was prepared in methanol. The adsorbed complex was eluted using methanol. The main band was collected, and the solution pH was lowered to 5.1 using 0.02 M nitric acid. Then, the solution containing the precipitate was kept at −20 °C for 15 h. After allowing the flask to warm to 25 °C, the precipitated complex was collected on a glass frit and air-dried. The same purification procedure was repeated two more times to obtain the pure nitrogen-bonded isomer complex. The NMR of the three times purified compound shows the presence of only one isomer containing 98.5% pure nitrogen-bonded thiocyanate ligands with one tetrabutylammonium cation.

The filtrate pH was further lowered to 4.0, and the flask was kept in a refrigerator for 12 h. The isolated product contains 80% of the sulfur-bonded isomer and 20% of the nitrogen-bonded isomer that was not characterized further.

^{1}H NMR (CD_3OD, dppm, *J*, Hz): 9.45 (2H, d, H^6, J = 5.8), 9.08 (2H, s, $H^{3'}$), 8.91 (2H, s, $H^{5'}$), 8.65 (2H, d, H^3), 8.01 (2H, dd, H^5, J = 6), 1.60 (18H, s, CH_3). Anal. Calcd for $C_{32}H_{30}N_6O_4S_2Ru$: C, 52.81; H, 4.15; N, 11.55. Found: C, 51.91; H, 4.32; N, 10.85.

3. Results and Discussion

3.1. Synthesis. To obtain a powerful convergent method, we designed a new Stille-based synthetic pathway to afford a series of quaterpyridyl ligands as shown in Scheme 1.

This method allows one to tune the substituent R in γ positions, and the key intermediate dimethyl 6,6′-dibromo-2,2′-bipyridine-4,4′-dicarboxylate permits the planning of the synthesis of a series of symmetric and nonsymmetric 4′,4″-disubstituted 2,2′:6′,2″:6″,2‴-quaterpyridine molecules (see Figure S1 in the Supporting Information). Scheme 2 shows all of the steps involved in synthesizing the dimethyl 4,4‴-di-*tert*-butyl-2,2′;6,2″;6″,2‴-quaterpyridine-4′,4″-dicarboxylate ligand in good yield.

The ruthenium complex N886 was synthesized in a one-pot synthesis starting from a dichloro(*p*-cymene)ruthenium-(II) dimer in DMF for 32 h. The crude complex NMR shows that it is a mixture of isomers, which were separated on a

(32) Nazeeruddin, M. K.; Péchy, P.; Renouard, T.; Zakeeruddin, S. M.; Humphry-Baker, R.; Comte, P.; Liska, P.; Le, C.; Costa, E.; Shklover, V.; Spiccia, L.; Deacon, G. B.; Bignozzi, C. A.; Graetzel, M. *J. Am. Chem. Soc.* **2001**, *123*, 1613.

Scheme 2. Step-by-Step Details for the Synthesis of Dimethyl 4,4‴-Di-*tert*-butyl-2,′:6′,2″:6″,2‴-quaterpyridine-4′,4″-dicarboxylate

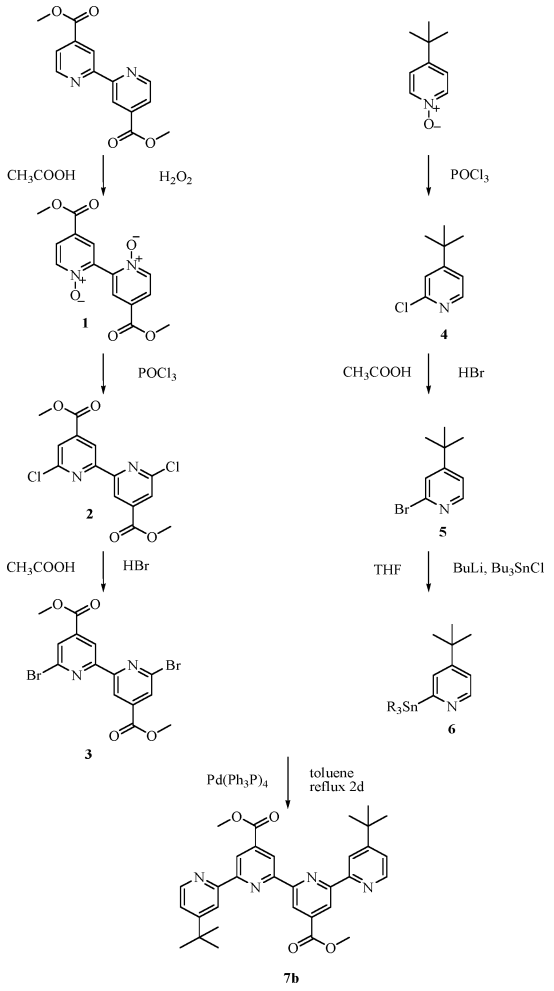

Sephadex LH-20 column using methanol as an eluent. The analytical and spectroscopic data for N886 are fully consistent with the structure (Figure 1) containing nitrogen-bonded thiocyanate ligands.

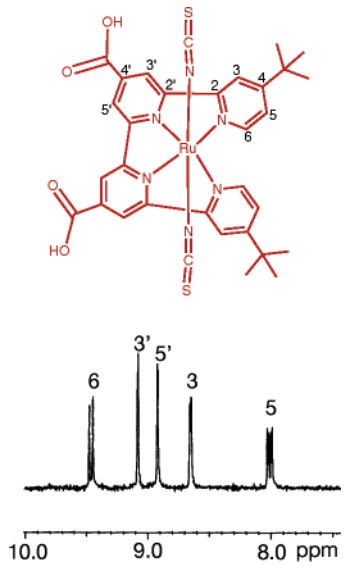

Figure 1. Part of a 200-MHz ^{1}H NMR spectrum of the N886 complex in CD_3OD. For clarity, the peaks in the aliphatic region are not included. The numbering scheme shows the assignment of various protons.

3.2. NMR Data. Figure 1 shows the NMR spectrum of the N886 complex, measured in a CD_3OD solution, which shows five well-resolved signals in the aromatic region, corresponding to the pyridyl protons in which the halves are magnetically equivalent. In an octahedral geometry, the tetradentate ligand (L) coordinates to a metal center in a plane and the thiocyanate ligands are in axial positions. The lowest-field doublet centered at δ 9.45 is assigned to the H^6 proton of the peripheral pyridine. The two singlets at δ 9.08 and 8.91 are due to the $H^{3'}$ and $H^{5'}$ protons of the central two pyridines of 4,4‴-di-*tert*-butyl-2,2′;6,2″;6″,2‴-quaterpyridine-4′,4″-dicarboxylic acid. The singlet and doublet centered at δ 8.65 and 8.01 are due to the H^3 and H^5 protons, respectively, due to the peripheral pyridines of 4,4‴-di-*tert*-butyl-2,2′;6,2″;6″,2‴-quaterpyridine-4′,4″-dicarboxylic acid.[33] In the aliphatic region, a singlet centered at δ 1.6 is assigned to the methyl proton *tert*-butyl group. The NMR data unambiguously confirm the absence of linkage isomers in the N886 complex, which were present in the crude complex to the extent of 25−35%.

3.3. Attenuated Total Reflection Fourier Transform IR Spectroscopy (ATR-FTIR) Spectra. The ATR-FTIR spectra of the N886 complex were measured as a solid and in the adsorbed form onto TiO_2 films. The N886 solid sample shows a strong band at 1710 cm^{-1} due to ν(C═O) and an intense peak at 1226 cm^{-1} due to the ν(C−O) stretch of the carboxylic acid groups. The band at 2097 cm^{-1} is due to ν(CN) and that at 795 cm^{-1} to ν(CS) of thiocyanate, indicating that it is coordinated to the ruthenium center through the nitrogen atom. The bands at 1606, 1562, 1529, and 1472 cm^{-1} are due to the ring-stretching modes of the ligand.[34] The *tert*-butyl stretching modes are located at 2873, 2931, and 2963 cm^{-1}.[35] The spectrum shows a broad band at 3371 cm^{-1} due to ν(O−H) water molecules.[36]

The ATR-FTIR data of the N886 complex anchored onto a 2-mm-thick nanocrystalline TiO_2 film reveal the mode of adsorption of this dye onto the TiO_2 surface. The ATR-FTIR spectra of the adsorbed N886 complex show clearly the absence of 1710 and 1226 cm^{-1} bands, which are due to a carboxylic acid group. However, the presence of the carboxylate asymmetric at $\nu(-COO^-_{as})$ 1613 cm^{-1} and the symmetric at $\nu(-COO^-_{s})$ 1354 cm^{-1} stretching vibrations corroborates that the carboxylic acid protons are dissociated and involved in the adsorption on the TiO_2 surface. The ring stretching mode of the adsorbed complex moved to 1599, 1537, and 1479 cm^{-1}, whereas the ν(CN) of the thiocyanate band remained unchanged compared to the solid IR spectra. The *tert*-butyl stretching modes (2875, 2935, and 2968 cm^{-1}) are shifted to higher energy in the adsorbed N886 complex compared to the solid. From the data of the adsorbed N886 complex, one infers that the dye is anchored on the surface through the carboxylate groups.[37]

(33) Constable, E. C.; Elder, S. M.; Healy, J.; Tocher, D. A. *J. Chem. Soc., Dalton Trans.* **1990**, 1669.
(34) Finnie, K. S.; Bartlett, J. R.; Woolfrey, J. L. *Langmuir* **1998**, *14*, 2744.
(35) Nakamoto, K. *Infrared and Raman spectra of inorganic coordination compounds*, 5th ed.; Wiley International Publication: New York, 1997.
(36) Colthup, N. B.; Daly, L. H.; Wiberley, S. E. *Introduction to Infrared and Raman Spectroscopy*; Academic Press: New York, 1964.
(37) Fillinger, A.; Parkinson, B. A. *J. Electrochem. Soc.* **1999**, *146*, 4559.

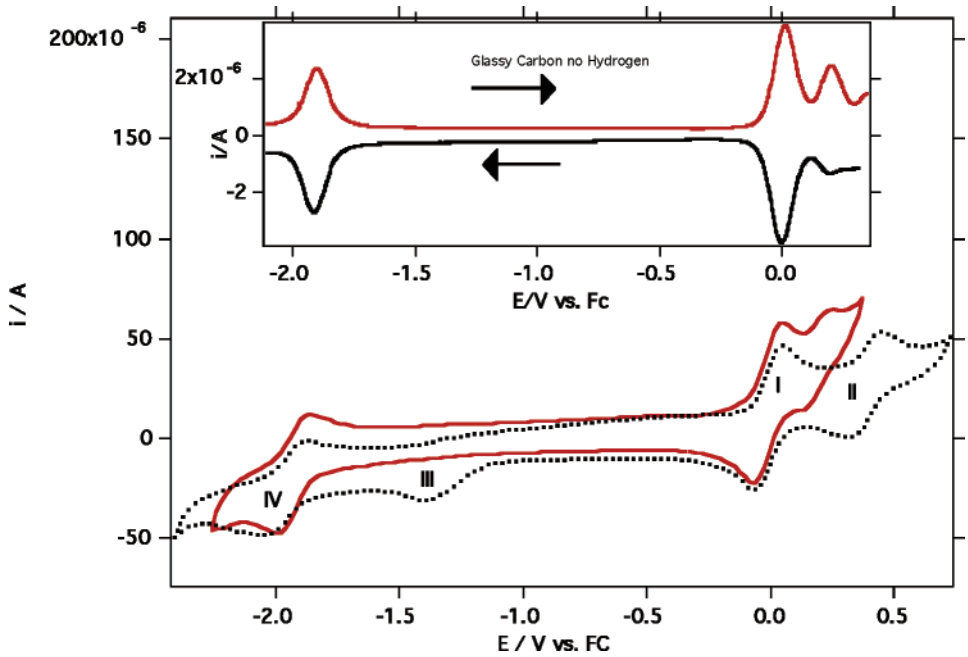

Figure 2. CV of the N886 complex in protonated (black line) and deprotonated states (red line) measured in a DMF solution containing 0.1 M TBA(PF_6) using a glassy carbon electrode with a scan rate of 500 mV/s. The redox couple labeled as **I** is due to Fc/Fc^+, which is used as an internal standard, **II** is ruthenium(III)/ruthenium(II), **III** is due to proton reduction, and **IV** is due to ligand reduction. The inset shows a differential pulse voltammogram of the N886 complex in the deprotonated state measured in a DMF solution containing 0.1 M TBA(PF_6) using a glassy carbon electrode with Fc as an internal reference. The direction of the measurement is shown with arrows (from negative to positive potentials, red curve; from positive to negative potentials, black curve), with a step potential of 10 mV, a modulation amplitude of 25 mV, a modulation time of 0.05 s, and an interval time of 0.5 s.

3.4. Electrochemistry. The CV of the N886 complex on a glassy carbon disk electrode is shown in Figure 2. Upon scanning to positive potentials, the N886 complex exhibited a quasi-reversible metal-centered oxidation, $E_{1/2} = 0.38$ V vs Fc^+/Fc reference couple with a separation of 120 mV between the anodic and cathodic peaks (Figure 2). Such a redox process is assigned to the ruthenium(II)/ruthenium(III) couple; however, the features of the CV indicate that it is followed by other irreversible oxidation, likely of the thiocyanate ligand. For the metal- and ligand-centered redox process, the anodic peak currents in the CV are proportional to the square root of the scan rate ($\nu^{1/2}$), which indicates that the peak current is a diffusion-controlled redox process (see Figures S2 and S3 in the Supporting Information). At negative potentials, an irreversible reduction wave (labeled as III in Figure 2a) appeared at −1.39 V, which is due to the reduction of protons on the carboxylic acid of 4,4‴-di-*tert*-butyl-2,2′;6,2″;6″,2‴-quaterpyridine-4′,4″-dicarboxylic acid. Wolfbauer et al. have observed a similar behavior of the protons of the $dcbpyH_2$ ligand in the N3 complex at a platinum electrode.[38] The quasi-reversible wave at $E_{1/2} = -1.93$ V vs Fc is assigned to the reduction of the 4,4‴-di-*tert*-butyl-2,2′;6,2″;6″,2‴-quaterpyridine-4′,4″-dicarboxylic acid ligand (wave IV). Upon deprotonation of the complex by treatment with tetrabutylammonium hydroxide or by electrochemical reduction of the protons to hydrogen, the irreversible couple III disappeared, accompanied by a quasi-reversible wave IV. The ligand-based reduction couple in the deprotonated form compares with that of the protonated form. Therefore, the origin of the irreversible peak is explicitly attributed to the reduction of the protons to hydrogen.

The ruthenium(III)/ruthenium(II) oxidation potential is shifted 180 mV cathodically in the deprotonated N886 complex compared to the protonated complex (see Figure 2) because of destabilization of the highest occupied molecular orbitals (HOMOs), as discussed in the Computational Study section. The ligand-based reduction potential in both protonated and deprotonated states is observed at the same potential of −1.93 V vs Fc. It should be mentioned that the UV−vis absorption spectra and the calculations show that the lowest unoccupied MOs (LUMOs) in the deprotonated N886 complex are destabilized compared to the protonated N886 complex. Nevertheless, electrochemical reduction potentials of both the protonated and deprotonated complexes show −1.93 V vs Fc. This is due to the fact that the protons in protonated species get reduced to hydrogen before ligand reduction takes place; therefore, identifying the protonated species reduction potential is not feasible.

3.5. Electronic Spectroscopy. The absorption spectrum of the N886 sensitizer, reported in Figure 3, is dominated in the visible region by absorption features at 382 (sh), 465, 515 and 637 nm and in the UV region by features at 240, 288, 301 (sh), 327, 341, and 359 nm. The bands in the visible and UV regions are generally assigned to metal-to-ligand charge-transfer (MLCT) transitions and to ligand $\pi-\pi^*$ charge-transfer transitions of 4,4‴-di-*tert*-butyl-2,2′;6,2″;6″,2‴-quaterpyridine-4′,4″-dicarboxylic acid,[39] respectively; see the

(38) Wolfbauer, G.; Bond, A. M.; Deacon, G. B.; MacFarlane, D. R.; Spiccia, L. *J. Am. Chem. Soc.* **2000**, *122*, 130.

(39) Ryan, M. F.; Metcalfe, R. A.; Lever, A. B. P.; Haga, M.-A. *J. Chem. Soc., Dalton Trans.* **2000**, 2357.

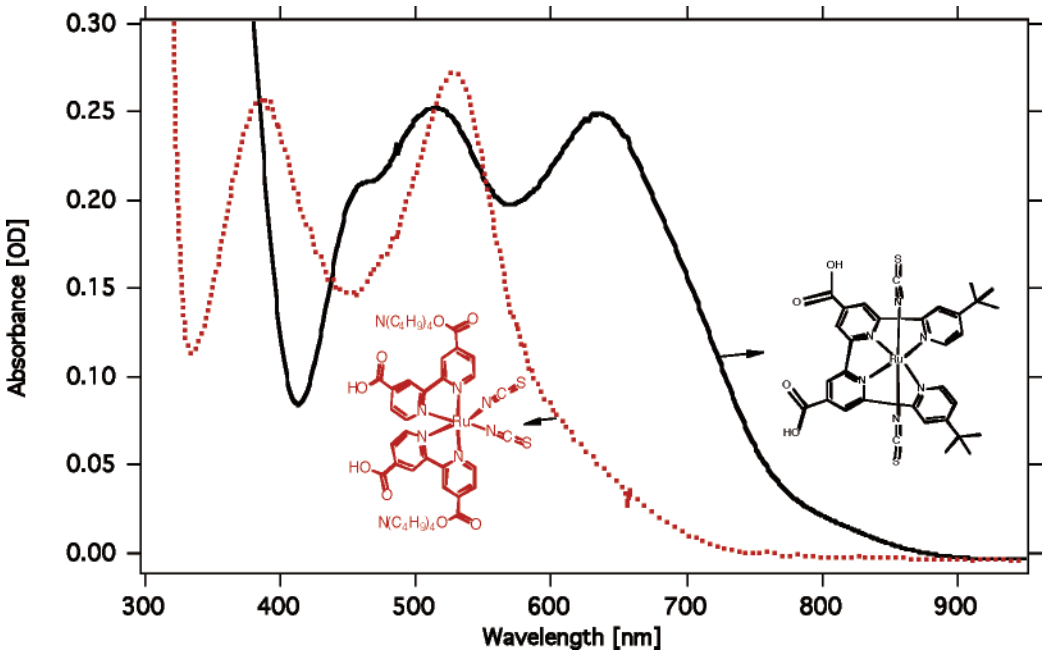

Figure 3. UV−vis absorption spectra of N886 (concentration 3.5×10^{-5}) and N719 (concentration 2.0×10^{-5}) complexes measured in an ethanol solution and their chemical structures.

Computational Study section for a detailed band assignment. The lowest-energy MLCT band in the N886 complex is red-shifted by 107 nm when compared to the standard N719 sensitizer (Figure 3). The $\pi-\pi^*$ charge-transfer bands and the low-energy MLCT bands of N886 shifted to higher energy by 37 nm upon deprotonation of the carboxylic groups (see Figure S3 in the Supporting Information). The blue shift is due to destabilization of both the HOMO and LUMO orbitals, causing the blue shifts of $\pi-\pi^*$ and $d\pi-\pi^*$ transitions to occur at higher energies.[12] The absorption spectra of N886 adsorbed on a 5-μm TiO_2 film show features similar to those seen in the corresponding solution spectra of the protonated species due to the interaction of the anchoring groups with the TiO_2 surface.[40]

4. Computational Study

The electronic and optical properties of the N886 complex, in its protonated and deprotonated forms, have been investigated by means of density functional theory (DFT) and time-dependent DFT (TDDFT) calculations in solution. Calculations have been performed using the B3LYP exchange-correlation functional,[41] as implemented in the *Gaussian03* (G03) program package.[42]

The geometries of the ruthenium(II) complexes were optimized in water without any symmetry constraints using the 3-21G* basis set.[43] Moreover, to evaluate the effects of solvation and of the basis set quality on the geometry, we optimized the geometry of the protonated N886 in vacuo using three different basis sets: (1) the same 3-21G* basis set as that used for geometry optimizations in solution; (2) a LANL2DZ[44a] basis set along with the corresponding pseudopotential[44b] for ruthenium (28 core electrons) and a 6-31G*[45] basis set for the remaining atoms; (3) an SDD[44c] basis set along with the quasi-relativistic MWB (28 core electrons) pseudopotential[44d] for ruthenium and a 6-31G* basis set for the remaining atoms. For computational convenience, we replaced the *tert*-butyl groups of the experimental N886 complex by smaller methyl groups. We separately checked that this substitution does not lead to appreciable changes in the electronic structure. Solvation effects were included by means of the conductor-like polarizable continuum model,[46] together with its nonequi-

(40) Klein, C.; Nazeeruddin, M. K.; Liska, P.; Censo, D. D.; Hirata, N.; Palomares, E.; Durrant, J. R.; Graetzel, M. *Inorg. Chem.* **2005**, *44*, 178.
(41) Becke, A. D. *J. Chem. Phys.* **1993**, *98*, 5648.
(42) Frisch, M. J.; Trucks, G. W.; Schlegel, H. B.; Scuseria, G. E.; Robb, M. A.; Cheeseman, J. R.; Montgomery, J. A., Jr.; Vreven, T.; Kudin, K. N.; Burant, J. C.; Millam, J. M.; Iyengar, S. S.; Tomasi, J.; Barone, V.; Mennucci, B.; Cossi, M.; Scalmani, G.; Rega, N.; Petersson, G. A.; Nakatsuji, H.; Hada, M.; Ehara, M.; Toyota, K.; Fukuda, R.; Hasegawa, J.; Ishida, M.; Nakajima, T.; Honda, Y.; Kitao, O.; Nakai, H.; Klene, M.; Li, X.; Knox, J. E.; Hratchian, H. P.; Cross, J. B.; Bakken, V.; Adamo, C.; Jaramillo, J.; Gomperts, R.; Stratmann, R. E.; Yazyev, O.; Austin, A. J.; Cammi, R.; Pomelli, C.; Ochterski, J. W.; Ayala, P. Y.; Morokuma, K.; Voth, G. A.; Salvador, P.; Dannenberg, J. J.; Zakrzewski, V. G.; Dapprich, S.; Daniels, A. D.; Strain, M. C.; Farkas, O.; Malick, D. K.; Rabuck, A. D.; Raghavachari, K.; Foresman, J. B.; Ortiz, J. V.; Cui, Q.; Baboul, A. G.; Clifford, S.; Cioslowski, J.; Stefanov, B. B.; Liu, G.; Liashenko, A.; Piskorz, P.; Komaromi, I.; Martin, R. L.; Fox, D. J.; Keith, T.; Al-Laham, M. A.; Peng, C. Y.; Nanayakkara, A.; Challacombe, M.; Gill, P. M. W.; Johnson, B.; Chen, W.; Wong, M. W.; Gonzalez, C.; Pople, J. A. *Gaussian 03*, revision B.05; Gaussian, Inc.: Wallingford, CT, 2004.
(43) Binkley, J. S.; Pople, J. A.; Hehre, W. J. *J. Am. Chem. Soc.* **1980**, *102*, 939.
(44) (a) Dunning, T. H.; Hay, P. J. In *Modern Theoretical Chemistry*; Schaefer, H. F., III, Ed.; Plenum: New York, 1976; Vol. 3, pp 1−28. (b) Hay, P. J.; Wadt, W. R. *J. Chem. Phys.* **1985**, *82*, 270. (c) Fuentealba, P.; Preuss, H.; Stoll, H.; Szentpaly, v. L. *Chem. Phys. Lett.* **1989**, *89*, 418. (d) Andrae, D.; Haeussermann, U.; Dolg, M.; Stoll, H., Preuss, H. *Theor. Chim. Acta* **1990**, *77*, 123.
(45) Ditchfield, R.; Hehre, W. J.; Pople, J. A. *J. Chem. Phys.* **1971**, *54*, 724.
(46) (a) Barone, V.; Cossi, M. *J. Phys. Chem. A* **1998**, *102*, 1995−2001. (b) Cossi, M.; Rega, N.; Scalmani, G.; Barone, V. *J. Comput. Chem.* **2003**, *24*, 669.

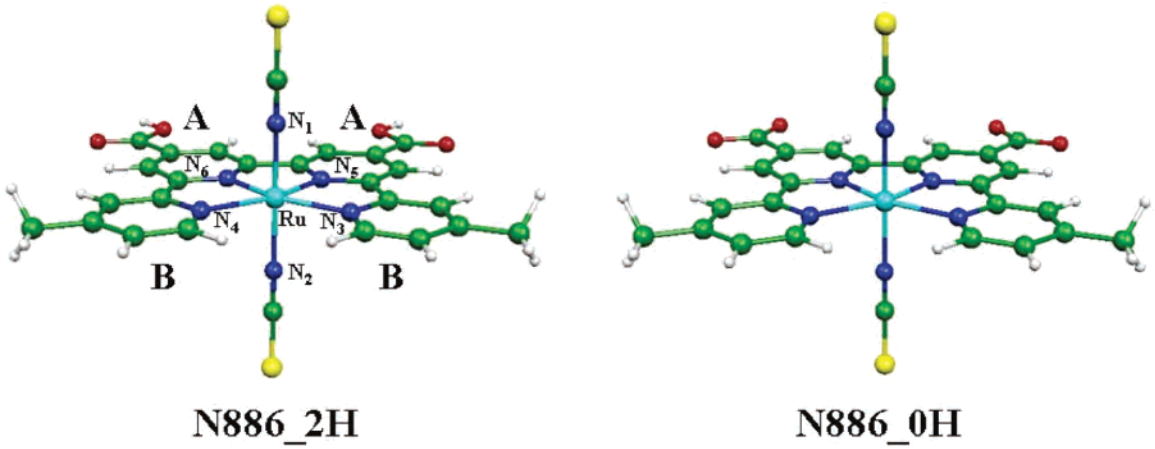

Figure 4. Optimized molecular structures of the investigated complexes. N886_2H and N886_0H refer to the protonated and deprotonated species, respectively.

librium version[47] for TDDFT calculations. TDDFT calculations in solution usually provide excitation spectra for N3-type sensitizers in good agreement with the experiment.[48,49] We notice, however, that recent theoretical analyses[50] have shown that the linear-response approach underlying TDDFT is not entirely satisfactory when including solvation effects with respect to state-specific methodologies. Therefore, a careful comparison with the experiment is performed to validate the theoretical data.

Electronic structural analysis and TDDFT calculations of the absorption spectra were performed in an ethanol solution using the larger DGDZVP basis set.[51] We computed the lowest 55 singlet−singlet transitions up to a wavelength of ca. 270 nm. We hereafter label the pyridines of the quaterpyridine ligand bearing the carboxylic groups as A, while those para-substituted by a methyl group are labeled as B, as shown in Figure 4.

4.1. Geometries and Electronic Structure. Optimized geometrical structures of the protonated and deprotonated N886 species are reported in Figure 4, while a comparison between the main geometrical parameters optimized using different basis sets in vacuo and in a water solution is shown in Table 1.

The optimized structures of both the protonated and deprotonated N886 complexes show an almost symmetric arrangement of the ligands; in Table 1, we therefore report average values. Notably, for the protonated complex, we find negligible differences between the geometries optimized with the three basis sets in vacuo; the largest deviations in the bond lengths and angles are within 0.01 Å and 0.7°,

Table 1. Comparison between the Main Optimized Geometrical Parameters (Bond Lengths in Angstroms and Angles in Degrees) Obtained with a 3-21G* Basis Set in Vacuo, a 3-21G* Basis Set in Water, 6-31G*/LANL2DZ in Vacuo, and a 6-31G*/SDD Basis Set in Vacuo for the Protonated N886 Species

	3-21G* in water	in vacuo		
		3-21G*	6-31G*/LANL2DZ	6-31G*/SDD
Ru−$N_1(N_2)$	2.057	2.038	2.045	2.032
$N_1(N_2)$−C	1.180	1.188	1.185	1.185
C−S	1.646	1.622	1.628	1.626
Ru−$N_3(N_4)$	2.191	2.191	2.200	2.184
Ru−$N_5(N_6)$	1.972	1.954	1.958	1.947
N_3−Ru−N_4	122.5	122.1	122.8	121.9
N_5−Ru−N_6	81.5	81.9	81.9	82.0

respectively. Going from the 3-21G* basis set to the 6-31G*/LANL2DZ basis set leads to a slight increase in the calculated Ru−N distances. On the other hand, adding quasi-relativistic corrections via the MWB28 pseudopotential with the 6-31G*/SDD basis set leads to a small reduction of the calculated Ru−N bond lengths with respect to the 6-31G*/LANL2DZ results, bringing the 6-31G*/SDD results closer to the 3-21G* ones. This confirms the adequacy of the 3-21G* basis set for geometry optimization, as was already found for related ruthenium(II) complexes,[48e,49,52] even though the 3-21G* good performances might be due to some error cancellation. Notably, inclusion of solvation effects, on the other hand, leads to slightly larger changes (within 0.02 Å) in the bond lengths. On the basis of these considerations, we used the geometries optimized using the 3-21G* basis set in a water solution throughout the paper.

For the protonated N886 species, the Ru−$N_1(N_2)$, Ru−$N_3(N_4)$, and Ru−$N_5(N_6)$ distances calculated at the 3-21G* level in a water solution are 2.057, 2.191, and 1.972 Å, respectively; these parameters shift to 2.060, 1.982, and 2.197 Å in the deprotonated species, probably as a result of the decreased π back-donation from the metal to the destabilized π^* orbitals of the tetradentate ligand (see below). A comparison of the optimized parameters of the protonated N886 with those calculated at the same level of theory for the N719 complex[49] shows that shorter Ru−N(CS) bond

(47) Cossi, M.; Barone, V. *J. Chem. Phys.* **2001**, *115*, 4708.
(48) (a) Guillemoles, J.-F.; Barone, V.; Joubert, L.; Adamo, C. *J. Phys. Chem. A* **2002**, *106*, 11354. (b) Fantacci, S.; De Angelis, F.; Selloni, A. *J. Am. Chem. Soc.* **2003**, *125*, 4381. (c) De Angelis, F.; Fantacci, S.; Selloni, A. *Chem. Phys. Lett.* **2004**, *389*, 204. (d) De Angelis, F.; Fantacci, S.; Selloni, A.; Nazeeruddin, M. K. *Chem. Phys. Lett.* **2005**, *415*, 115.
(49) Nazeeruddin, M. K.; De Angelis, F.; Fantacci, S.; Selloni, A.; Viscardi, G.; Liska, P.; Ito, S.; Takeru, B.; Grätzel, M. *J. Am. Chem. Soc.* **2005**, *127*, 16835.
(50) (a) Cammi, R.; Corni, S.; Mennucci, B.; Tomasi, J. *J. Chem. Phys.* **2005**, *122*, 104513. (b) Corni, S.; Cammi, R.; Mennucci, B.; Tomasi, J. *J. Chem. Phys.* **2005**, *123*, 134512.
(51) Godbout, N.; Salahub, D. R.; Andezelm, J.; Wimmer, E. *Can. J. Chem.* **1992**, *70*, 560.
(52) Fantacci, S.; De Angelis, F.; Sgamellotti, N.; Re, N. *Chem. Phys. Lett.* **2004**, *396*, 43.

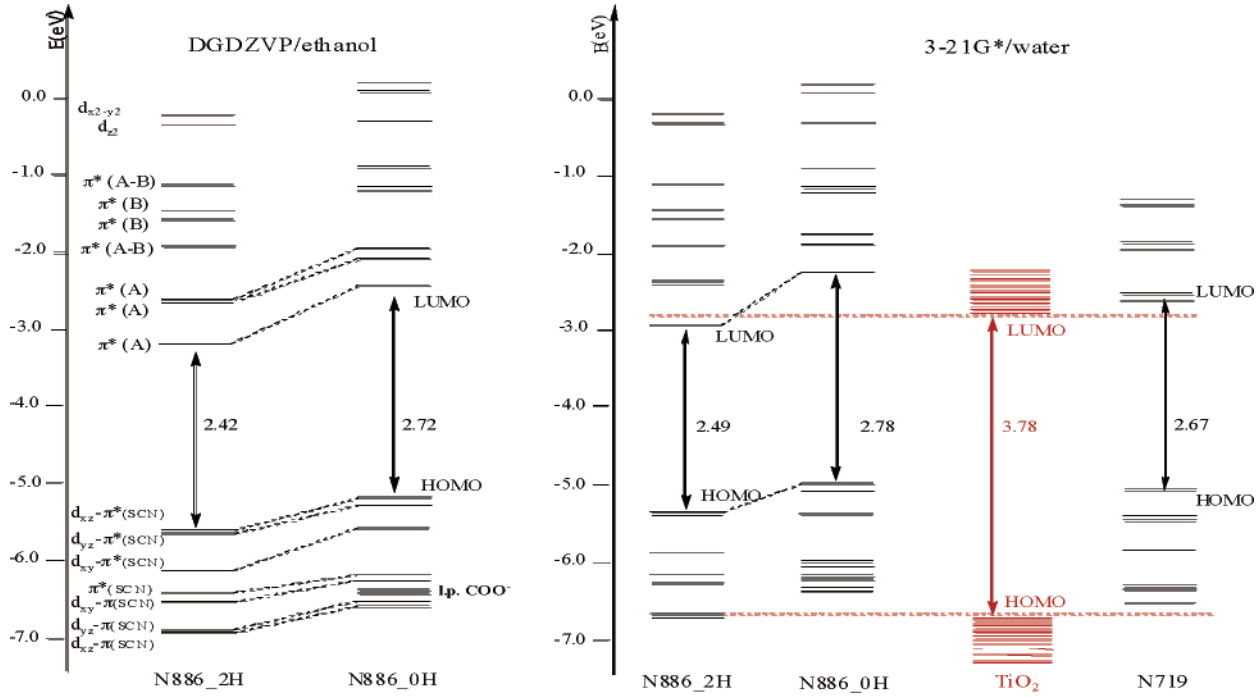

Figure 5. Left panel: schematic representation of the MO energies for the protonated and deprotonated N886 species. N886_2H and N886_0H refer to the protonated and deprotonated species, respectively. Results obtained with the DGDZVP basis set in ethanol are reported. Right panel: schematic representation of the MO energies for the protonated N886_2H and deprotonated N886_0H species, compared to results obtained for the N719 complex[49] and for a model TiO_2 nanoparticle.[54] Results obtained with the 3-21G* basis set in a water solution are reported.

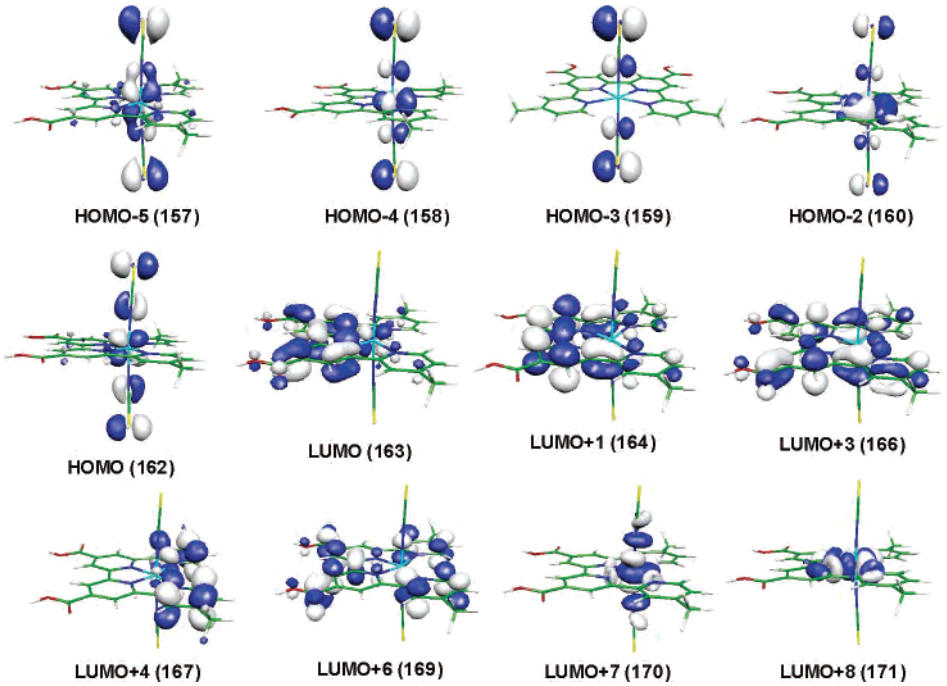

Figure 6. Isodensity plots of the frontier orbitals of the protonated N886. Similar orbital plots are obtained for the deprotonated species.

distances are calculated for the present N886 complex compared to N719 (2.057−2.060 vs 2.079−2.082 Å). This is the result of the stronger interaction between two trans thiocyanate ligands with respect to a thiocyanate ligand trans to a pyridine, as happens in the N719 cis complex.

A schematic orbital energy diagram of the investigated N886 complexes is reported in the left panel of Figure 5, while isodensity plots of the frontier orbitals of protonated N886 are shown in Figure 6. The seven HOMOs of N886 show contributions from both the ruthenium center and thiocyanate ligands in variable percentages. In particular, the first two almost degenerate HOMOs, lying within 0.04 eV, are antibonding combinations of the Ru d_{xz} and d_{yz} orbitals with the SCN π orbitals, while HOMO-2 and HOMO-4, lying 0.51 and 0.93 eV below the HOMO, respectively, are nonbonding d_{xy}−SCN π combinations, see Figure 6. HOMO-3, lying 0.80 eV below the HOMO, is a pure SCN π orbital, while the almost degenerate HOMO-5/HOMO-6 represent

the bonding counterpart of the $d_{xz}/d_{yz}(Ru)-\pi(SCN)$ orbitals and lie 1.32 eV below the HOMO. It is interesting to compare the electronic structure of the prototype cis N3 and N3-derived complexes,[48,49,53] with that of the trans N886 complex, subject of the present investigation. Both types of complexes show the seven highest HOMOs of mixed Ru−SCN character. In N3 and, in general, in *cis*-dithiocyanate-bipyridine complexes,[48,49,53] the seven HOMOs split into two bonding and antibonding $t_{2g}(Ru)-\pi(SCN)$ combinations, each composed of three almost degenerate orbitals and an isolated orbital of π(SCN) character. In the present N886 complex, on the other hand, the t_{2g}(Ru) orbitals are no longer degenerate so that the $d_{xy}(Ru)-\pi(SCN)$ orbitals (HOMO-2 and HOMO-4) are destabilized and stabilized with respect to the bonding and antibonding $d_{xz}/d_{yz}(Ru)-\pi(SCN)$ combinations, respectively.

The seven LUMOs of the protonated N886 complex are π^* combinations localized on the quaterpyridine ligand, while LUMO+7 and LUMO+8 have d_{z^2}(Ru) and $d_{x^2-y^2}$(Ru) character, respectively, and lie ca. 0.8 above LUMO+6. LUMO/LUMO+2 are mainly localized on the portion of the ligand bearing the carboxylic groups (A in Figure 4). In particular, the LUMO is localized on the pyridines bearing the carboxylic groups and on the C−C bond connecting them, while LUMO+1 and LUMO+2, lying 0.55 eV above the LUMO, have also amplitudes on the C−C bonds connecting the A and B pyridines; see Figure 6. LUMO+3 and LUMO+6, lying 1.27 and 2.06 eV above the LUMO, are completely delocalized over the tetradentate ligand; LUMO+4 and LUMO+5, found 1.62 eV above the LUMO, are localized on the two pyridines bearing the methyl groups (B in Figure 4). LUMO, LUMO+3, and LUMO+6 show contributions from the carboxylic groups.

The deprotonated N886 complex shows an electronic structure pattern similar to that discussed above for the protonated complex. The main difference with respect to the protonated species is that the HOMO−LUMO gap increases from 2.42 to 2.72 eV, due to a larger destabilization of the unoccupied with respect to the occupied orbitals. Moreover, deprotonation of N886 leads to the insertion of two oxygen lone pairs of the carboxylate groups among the seven $t_{2g}(Ru)-\pi(SCN)$ HOMOs. A comparison of the calculated HOMO−LUMO gaps with the corresponding quantity measured by electrochemical studies is not straightforward because the calculated values are approximations to vertical oxidation/reduction potentials, while the electrochemical redox potentials refer to adiabatic processes, in which both the oxidized and reduced species are at their equilibrium geometries. Nevertheless, the calculated value for the deprotonated species (2.72 eV) is not far from the experimental difference of redox potentials (2.13 V). Similar arguments apply to the trend of redox potentials on going from the protonated to the deprotonated N886 species. Indeed, in an ethanol solution, we calculate the HOMO of the protonated and deprotonated complexes to lie at −5.61 and −5.19 eV, respectively; this HOMO energy upshift (0.42 eV) upon deprotonation of N886 qualitatively correlates with the experimental trend of oxidation potentials, showing an increase of 0.180 mV upon deprotonation of the carboxylic groups.

4.2. Absorption Spectra. The calculated absorption spectra of the protonated and deprotonated N886 complexes are shown in Figure 7; the most representative calculated optical transitions for the protonated species are collected in Table 2, while a complete list of relevant calculated optical transitions for both complexes is available as Supporting Information. For the protonated N886, the calculated spectrum qualitatively agrees with the experimental one reported in Figure 3. In particular, the main absorption features of the experimental spectrum are reproduced by theory, despite a red shift of the lowest-energy band in the visible region of the spectrum. This band, experimentally found at 637 nm, is calculated at 699 nm, i.e., only 0.17 eV red-shifted with respect to the experimental data, and appears to be composed of two transitions at 731 and 672 nm, which originated from the HOMO-1/HOMO (Ru−SCN) couple to the LUMO (π^* on pyridines A). We therefore see that the lowest-energy band in the visible region originates an excited state of mixed Ru−SCN to quaterpyridine character, maximally localized on the ligand portion bearing the carboxylic groups, with sizable contributions from these groups. At shorter wavelengths, we calculate an intense band at 519 nm, whose position is in excellent agreement with the experimental value of 515 nm. This band is originated by three transitions of mixed MLCT character calculated at 539, 519, and 492 nm, all having as starting states the same HOMO-1/HOMO set but arriving at the higher-lying LUMO+1/LUMO+2 π^* orbitals, therefore appearing at higher energy with respect to the experimentally characterized 637 nm band. The experimental 465 nm band appears to be related to a mixed MLCT transition of sizable intensity calculated at 452 nm, involving as the starting orbital HOMO-4, of d_{xy} character, with the LUMO as the arriving state; see Table 2. We notice, however, that in the calculated spectrum this transition is hidden by the experimental 515 nm band, probably because of some inaccuracies in the calculated intensity distributions.[55] Our calculated spectrum reproduces also the appearance of the experimental 382 nm shoulder, this feature being related to two mixed MLCT transitions calculated at 398 and 394 nm having the same HOMO-1/HOMO set as starting states, with the arriving state LUMO+3, delocalized all over the tetradentate ligand.

Most notably, we calculate a set of mixed MLCT transitions also in the 360−330 nm region, which give rise to three closely spaced peaks experimentally found at 359, 341, and 327 nm. A similar behavior has been found in a previous study of a related trans complex.[39] These transitions have as starting states the same orbitals as those found for the lower-lying MLCT bands, whereas the arriving states are LUMO+3

(53) Rensmo, H.; Södergren, S.; Patthey, L.; Westmark, K.; Vayssieres, L.; Khole, O.; Brühwiler, P. A.; Hagfeldt, A.; Siegbahn, H. *Chem. Phys. Lett.* **1997**, *274*, 51.

(54) De Angelis, F.; Tilocca, A.; Selloni, A. *J. Am. Chem. Soc.* **2004**, *126*, 15024.

(55) Tozer, D. J.; Amos, R. D.; Handy, N. C.; Roos, B. O.; Serrano-Andres, L. *Mol. Phys.* **1999**, *97*, 859.

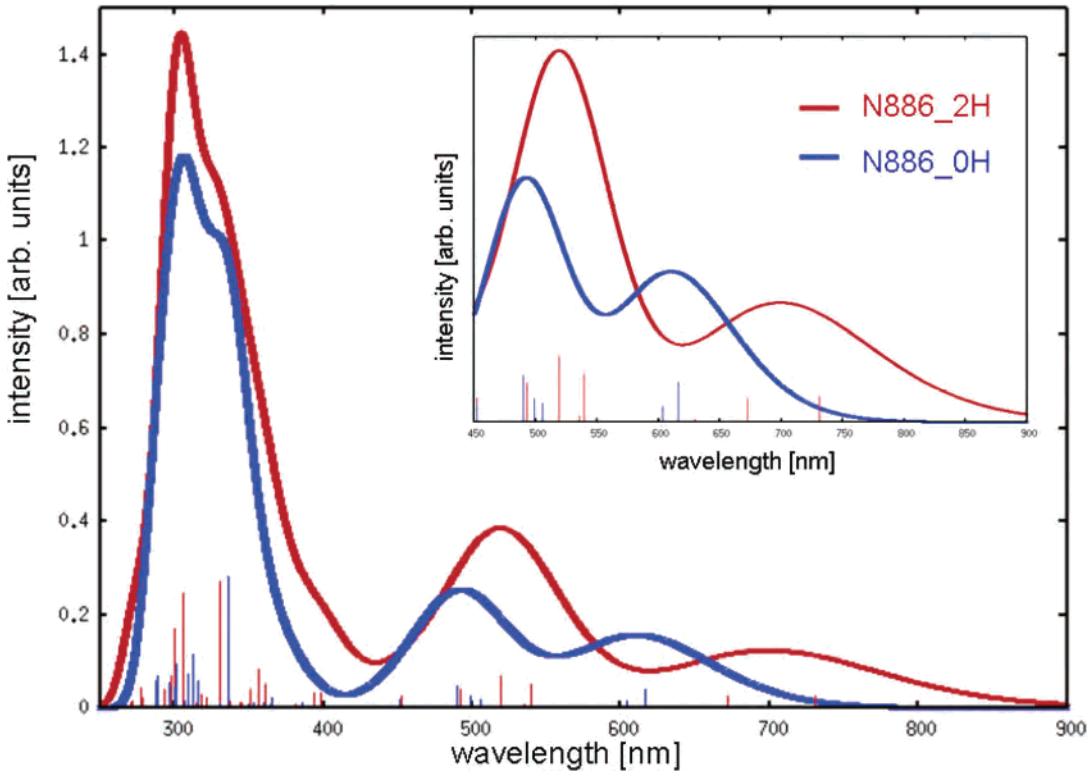

Figure 7. Computed absorption spectra and vertical excitation energies and oscillator strengths for the protonated and deprotonated N886. N886_2H and N886_0H refer to the protonated and deprotonated species, respectively. Inset: detail of the calculated spectra in the 450−900 nm region.

Table 2. Main Calculated Optical Transitions for the Protonated N886 Complex, with Oscillator Strength $f > 0.02$[a]

w (nm)	*f*	composition	character	theor. (nm)	exp. (nm)
731.03	0.0269	93% (HOMO-1 → LUMO)	MLCT	699	637
672.21	0.0244	83% (HOMO → LUMO)	MLCT		
539.43	0.0496	87% (HOMO → LUMO+2)	MLCT	519	515
518.78	0.0679	90% (HOMO-1 → LUMO+1)	MLCT		
492.28	0.0407	78% (HOMO-1 → LUMO+2)	MLCT		
452.00	0.0251	89% (HOMO-4 → LUMO)	MLCT	452	465
397.59	0.0344	95% (HOMO → LUMO+3)	MLCT	395 (sh)	382 (sh)
393.95	0.0311	76% (HOMO-1 → LUMO+3); 18% (HOMO-5 → LUMO)	MLCT; $\pi-\pi^*$		
360.42	0.0516	53% (HOMO-7 → LUMO); 38% (HOMO-1 → LUMO+4)	$\pi-\pi^*$; MLCT	358 (sh)	360
356.74	0.0840	53% (HOMO-1 → LUMO+4); 25% (HOMO-7 → LUMO); 16% (HOMO → LUMO+5)	MLCT; $\pi-\pi^*$; MLCT		
350.78	0.0414	78% (HOMO → LUMO+5)	MLCT	351	341
329.81	0.2702	63% (HOMO-6 → LUMO+1); 11% (HOMO-5 → LUMO+2)	MLCT; MLCT	330	327
321.69	0.0228	59% (HOMO-6 → LUMO+2); 10% (HOMO → LUMO+6)	MLCT; MLCT		
317.75	0.0297	88% (HOMO → LUMO+6)	MLCT		
305.25	0.2443	80% (HOMO-8 → LUMO)	$\pi-\pi^*$	304	288−301 (sh)
299.98	0.1708	69% (HOMO-7 → LUMO+2); 15% (HOMO-2 → LUMO+7)	$\pi-\pi^*$; d−d		
297.55	0.0678	54% (HOMO-2 → LUMO+7); 19% (HOMO-7 → LUMO+2)	d−d; $\pi-\pi^*$		

[a] Only orbital percentages larger than 10% are reported. We use for simplicity MLCT to label the mixed Ru−NCS to quaterpyridine π^*, as discussed in the text. A comparison between the computed and main experimental absorption features is also reported

and LUMO+5. In this wavelength range, there is also a weak component arising from d−d transitions (see Table S1 in the Supporting Information). The most intense transition among these high-energy MLCT features is calculated at 330 nm ($f = 0.2702$), involving as starting states the couple HOMO-5/HOMO-6 with LUMO as the arriving state; two much less intense transitions of the same character are also found at 337 and 322 nm (see Supporting Information and Table 2).

Still at higher energy (305 and 300 nm), we compute two intense transitions ($f = 0.2443$ and 0.1708, respectively) of essentially $\pi \rightarrow \pi^*$ character, which coincide with the maxi-

mum of the intense 288−301 nm features of the experimental spectrum. Two much less intense MLCT transitions from the HOMO/HOMO-1 to LUMO+6 are computed at 318 and 315 nm (see Table 2 and the Supporting Information), and a series of less intense transitions of mixed character (MLCT and $\pi \rightarrow \pi^*$) are found in the range 297−270 nm. At 298 nm, quite an intense ($f = 0.0678$) d−d transition is calculated. The intensity of the calculated spectrum in the region below 300 nm is underestimated with respect to the experimental one because of the limited number of transitions which could be evaluated.

The calculated absorption spectrum of the deprotonated N886 complex is similar to that of the protonated species, apart from a blue shift of all the main spectral features in the visible range. The MLCT features calculated at 731 and 672 nm in the protonated species now appear at 616 and 603 nm, even though they maintain the same mixed character (see the Supporting Information). The three transitions composing the 515 nm band of the protonated N886 experimental spectrum are now calculated at 506, 499, and 489 nm. Interestingly, also in the deprotonated case, we compute an isolated MLCT transition at 452 nm originating from a d_{xy} Ru orbital. The calculated spectral modifications upon deprotonation of the carboxylic groups are in good agreement with experimental data (see the Supporting Information), showing a decreasing blue shift of the main visible spectral features with decreasing wavelength. At higher energy, a similar pattern of MLCT and $\pi \rightarrow \pi^*$ transitions is calculated for the deprotonated species.

5. Photovoltaic Data

The N886-sensitized solar cells based on a double-layered nanocrystalline TiO_2 film with an electrolyte consisting of 0.60 M 1-propyl-3-methylimidazolium iodide, 0.03 M I_2, and 0.50 M *tert*-butylpyridine in a mixture of acetonitrile and valeronitrile (volume ratio 1:1) were tested. The incident monochromatic photon-to-current conversion efficiency (IPCE), plotted as a function of the excitation wavelength, shows a plateau region with yields of 40%. The N886-sensitized cell gave, under standard global AM 1.5 solar condition, a short-circuit photocurrent density (i_{sc}) of 11.80 ± 0.20 mA/cm^2, an open-circuit voltage (V_{oc}) of 680 ± 30 mV, and a fill factor (ff) of 0.73 ± 0.03, corresponding to an overall conversion efficiency η, derived from the equation $\eta = i_{sc}V_{oc}$ff, of 5.85%. The lower IPCE of N886 is likely to be partly due to the aggregation of the sensitizer on the TiO_2 surface, resulting in low short-circuit photocurrent density. The open-circuit voltage of N886 is 120 V lower than that of the N719 sensitizer, which could be due to the adsorption geometry of the sensitizer. It is interesting to note that for 40% IPCE the short-circuit current is 11.80 ± 0.20 mA/cm^2, which if we could improve to 89% similar to N719, then the short-circuit current would be around 25 mA/cm^2, resulting in close to 12.5% efficiency.

To gain insight into the electronic factors leading to the reduced photovoltaic efficiency of N886 with respect to the N719 complex, we analyze the alignment of the energy levels of the N886 and N719 dyes with those of a TiO_2 nanoparticle model, made of a $Ti_{38}O_{76}$ cluster of nanometric dimensions exposing 101 anatase surfaces.[54] For the sake of comparison, we now use homogeneous data obtained in a water solution at the B3LYP/3-21G* level of theory. Moreover, we check the effect of the basis set and solvent on the HOMO and LUMO energies of N719 and N886; see below. Data for the N719 complexes have been previously published.[49] The results are reported in the right panel of Figure 5.

For the bare $Ti_{38}O_{76}$ nanoparticle model, HOMO and LUMO are calculated at −6.55 and −2.77 eV, respectively, at the 3-21G* level in water, with a lowest TDDFT excitation energy of 3.2 eV,[52] in good agreement with typical band gaps of TiO_2 nanoparticles of a few nanometers in size.[56] For both the N886 and N719 dyes, the seven HOMOs are found to insert within the TiO_2 gap. However, while in the N886 complex the LUMO is computed to lie at −2.85 eV, i.e., 0.08 eV below the TiO_2 conduction band edge, for the N719 complex the LUMO is calculated at −2.63 eV, i.e., 0.14 eV above the TiO_2 conduction band edge. Our calculations therefore indicate that the N886 LUMO is destabilized by 0.22 eV with respect to the N719 LUMO at the 3-21G* level in a water solution. Remarkably, using the larger DGDZVP basis set, we calculate the N886 LUMO to be destabilized by 0.22 and 0.23 eV with respect to the N719 LUMO in ethanol and water solutions, respectively, essentially the same value as that calculated with the 3-21G* basis set in water. This confirms that the 3-21G* basis set provides the same relative LUMO alignment as the larger DGDZVP basis set and that changing the solvent does not significantly affect this alignment.

The lineup of N719 and N886 energy levels with the TiO_2 conduction band could explain why such a low IPCE is obtained with the N886 dye compared to the good values obtained with the N719 dye.[49] Indeed, the two excited states originating from the experimentally 637-nm absorption band in the protonated N886 complex involve essentially excitations to the LUMO (see Table 2), which, lying well below the TiO_2 conduction edge, could result in inefficient electron transfer to the semiconductor band states.

It has also to be noticed that, upon adsorption onto TiO_2, the dye could transfer some of its protons to the surface; according to the discussion presented above, one would expect the LUMO of the deprotonated dye to raise its energy, possibly above the TiO_2 conduction edge. We notice, however, that once adsorbed onto the TiO_2 surface, the dye would bind to the surface Ti^{4+} centers, thus lowering again the LUMO energy because of the interaction with the positive surface charges. At the same time, upon charging the TiO_2 surface positively with protons, the LUMO should decrease its energy, but adsorption of the anion in (deprotonated) dye should counterbalance this effect. This is effectively seen in

(56) (a) Yang, M.; Thompson, D. W.; Meyer, G. J. *Inorg. Chem.* **2000**, *39*, 3738. (b) Weng, Y. X.; Wang, Y. Q.; Asbury, J. B.; Ghosh, H. N.; Lian, T. *J. Phys. Chem. B* **2000**, *104*, 93. (c) Yang, M.; Thompson, D. W.; Meyer, G. J. *Inorg. Chem.* **2002**, *41*, 1254. (d) Khoudiakov, M.; Parise, A. R.; Brunschwig, B. S. *J. Am. Chem. Soc.* **2003**, *125*, 4637.

the absorption spectrum of the N886 dye adsorbed onto TiO_2, which shows the same characteristics of the protonated dye in solution.

6. Conclusions and Perspectives

The noteworthy feature of this work is success in developing a novel synthetic route for functionalized tetradentate ligands (see the Supporting Information) and the panchromatic sensitizer N886 based on ruthenium, which displays absorption bands in the entire visible and near-IR regions. A thorough characterization of the newly developed complex has been performed by combining experimental and high-level theoretical calculations. In particular, DFT and TDDFT calculations in solution have allowed a detailed understanding of the N886 electronic structure and absorption spectra. The enhanced spectral response of the N886 complex compared to that of the widely used N719 dye (see especially Figure 2) is expected to improve significantly the overall efficiency of a dye-sensitized solar cell. However, the disadvantage of N886 is the relatively low molar extinction coefficient of its MLCT bands compared to the N719 dye and the unfavorable alignment of its excited states with respect to the TiO_2 conduction band, as inferred from DFT calculations. Thus, this class of compounds serves as the basis for the design of novel compounds containing an extended π-system donor on 4 and 4′ positions and an extended π-system acceptor anchoring groups on the 4″ and 4‴ positions of 2,2′:6′,2″:6″,2‴-quaterpyridine, which are expected to have significantly increased molar extinction coefficients of low-energy MLCT bands and a favorable alignment of its excited states with respect to the TiO_2 conduction band. The panchromatic sensitizers with enhanced molar extinction coefficients allow a reduction in the film thickness, which should lead to increased open-circuit potentials and an overall efficiency of the solar cells. We are currently addressing the research directed toward this goal in our laboratory.

Acknowledgment. We acknowledge financial support of this work by the Swiss Science Foundation, Swiss Federal Office for Energy (OFEN), and U.S. Air Force Research Office under Contract No. F61775-00-C0003. We thank Dr. Robin Humphry-Baker and Takeru Bessho for their kind assistance. C.B., G.V., and P.Q. were supported by the University of Torino and are particularly grateful to Compagnia di San Paolo (Torino) and Fondazione della Cassa di Risparmio di Torino (Italy) for the supply of laboratory equipment.

Supporting Information Available: Synthesis of quaterpyridyl ligands, UV−vis absorption spectra of N886 and N3 complexes, and calculated vertical excitation energies and oscillator strengths. This material is available free of charge via the Internet at http://pubs.acs.org.

IC051970W